Unified potential fluctuations model for photoluminescence spectra at room temperature-Cu(In,Ga)Se_2thin films

Spaans, E. M.; De Wild, J.; Savenije, T. J.; Vermang, B.

DOI
10.1063/5.0056629

Publication date
2021

Document Version
Final published version

Published in
Journal of Applied Physics

Journal of Applied Physics

Unified potential fluctuations model for photoluminescence spectra at room temperature—Cu(In,Ga)Se_2 thin films

Cite as: J. Appl. Phys. **130**, 123103 (2021); https://doi.org/10.1063/5.0056629
Submitted: 12 May 2021 • Accepted: 10 September 2021 • Published Online: 28 September 2021

E. M. Spaans, J. de Wild, T. J. Savenije, et al.

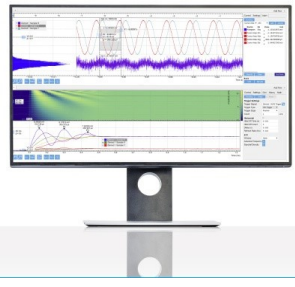

AIP Publishing

Journal of Applied Physics ARTICLE scitation.org/journal/jap

Unified potential fluctuations model for photoluminescence spectra at room temperature—Cu(In,Ga)Se_2 thin films

Cite as: J. Appl. Phys. **130**, 123103 (2021); doi: 10.1063/5.0056629
Submitted: 12 May 2021 · Accepted: 10 September 2021 ·
Published Online: 28 September 2021

E. M. Spaans,[1] J. de Wild,[2,3,4,a)] T. J. Savenije,[1] and B. Vermang[2,3,4]

AFFILIATIONS

[1]Department of Chemical Engineering, Delft University of Technology, 2629 HZ Delft, The Netherlands
[2]Institute for Material Research (IMO), Hasselt University (Partner in Solliance), Wetenschapspark 1, 3590 Diepenbeek, Belgium
[3]IMOMEC, imec (Partner in Solliance), Wetenschapspark 1, 3590 Diepenbeek, Belgium
[4]EnergyVille 2, Thor Park 8320, 3500 Genk, Belgium

[a)]**Author to whom correspondence should be addressed:** Jessica.deWild@imec.be

ABSTRACT

Room temperature photoluminescence (PL) is a powerful technique to study the properties of semiconductors. However, the interpretation of the data can be cumbersome when non-ideal band edge absorption takes place, as is the case in the presence of potential fluctuations. In this study, PL measurements are modeled to quantify potential fluctuations in Cu(In,Ga)Se_2 (CIGS) absorber layers for photovoltaic applications. Previous models have attributed these variations to either bandgap fluctuations (BGFs) or electrostatic fluctuations (EFs). In reality, these two phenomena happen simultaneously and, therefore, affect the PL together. For this, the unified potential fluctuation (UPF) model is introduced. This model incorporates the effect of both types of fluctuations on the absorptance of the material and subsequently the PL spectra. The UPF model is successfully used to fit both single- and three-stage co-evaporated ultrathin (around 500 nm) CIGS samples, showing a clear improvement with respect to the previous BGF and EF models. Some PL measurements show possible interference distortions for which an interference function is used to simultaneously correct the PL spectra of a sample measured with several laser excitation intensities. All the models used in this work are bundled into a user-friendly, open-source Python program.

I. INTRODUCTION

The ambition of achieving a carbon-free society is paving the way for continuous developments in photovoltaics. With crystalline silicon increasingly dominating the market share, thin-film technologies must continue to evolve in order to compete with this established industry, both from a performance and an economical perspective. Within thin-film photovoltaics, Cu(In,Ga)Se_2 (CIGS) is seen as one of the most promising materials,[1] already reaching a 23.4% efficiency on a cell level.[2,3] One of the key challenges to push the efficiency further is to understand and control the electronic properties of the absorber layer,[4] given its inherent electronic inhomogeneities that degrade the V_{oc},[5,6] for instance.

Proper characterization techniques are indispensable to evaluate the electronic quality of absorber layers and to identify opportunities for improvement. In this regard, photoluminescence (PL) is a resourceful method to investigate the optoelectronic properties of a semiconductor. The possibility of changing experimental parameters such as the temperature and excitation intensity allows the exploration of diverse material characteristics such as the bandgap, defect distribution, quasi-Fermi level splitting, and potential variations,[7] among others. There are extensive PL studies on chalcopyrite materials that examine these parameters. Measurements at low temperatures have been performed to identify the ionization energies of defect levels[8,9] and spatial variations of the quasi-Fermi level splitting,[10] as well as absolute values of this splitting energy at room temperature.[11] Moreover, the positive effect of KF post-deposition treatments was quantified from PL measurements by noting a reduction in potential fluctuations at low temperature PL[12] and reduced sub-bandgap absorption in room temperature PL.[13]

The inhomogeneity of CIGS has been confirmed through spatially resolved PL. With submicrometer lateral resolution measurements, fluctuations of the quasi-Fermi level splitting[14] and local bandgaps[15] have been identified, the last one being attributed to local changes of composition.[16,17] To relate these electrical properties to PL spectra, the generalized Planck's law is often used, which links the energy-dependent photon emission $\phi_{PL}(E)$ to the external rate of spontaneous emission under non-equilibrium conditions, given by[18]

$$\phi_{PL}(E) = \frac{2\pi}{h^3c^2}\frac{a(E)E^2}{\exp\left(\frac{E-\Delta\mu}{k_B T}\right)-1}, \quad (1)$$

where h is Planck's constant, c the speed of light, $a(E)$ the absorptance, $\Delta\mu$ the quasi-Fermi level splitting, k_B the Boltzmann constant, and T the absolute temperature. This relation holds for constant material properties and $\Delta\mu$.[7] To compute the quasi-Fermi level splitting, it can be assumed that for E well above the bandgap E_g, $a(E) = 1$ such that the equation can be simplified to obtain $\Delta\mu$ as a function of ϕ_{PL}. This provides an upper limit for the open-circuit voltage V_{oc}.[7] Nevertheless, it has been shown that this high-energy tail fitting procedure is very sensitive to the fitting region.[19] This could lead to reasonable differences in the obtained $\Delta\mu$ and must, therefore, be used carefully.

Other approaches to the use of Eq. (1) involve modeling the absorptance $a(E)$ in an attempt to fit the resulting PL spectrum. Given the inhomogeneous nature of CIGS, potential fluctuations arising from bandgap fluctuations (BGFs) and electrostatic fluctuations (EFs) are present in such polycrystalline absorbers.[6] These two are visualized in Fig. 1. For BGF [Fig. 1(a)], the conduction and valence band edges vary independently, changing the local bandgap throughout the material. Moreover, the vacuum level is constant. Here, we can define a global, average bandgap: $\bar{E}_g$. For EF [Fig. 1(b)], the conduction band and valence band edges, as well as the vacuum level, vary synchronously, keeping the band gap E_g constant. In both cases, the maximum quasi-Fermi level splitting $\Delta\mu_{max}$ of the material is reduced, limiting the V_{oc} of the resulting cell.[4] Moreover, the absorptance profile is also affected, and models that deviate from an ideal absorptance must, therefore, be used. Some approaches that include sub-bandgap absorption have been proposed. On the one hand, BGF can be modeled with a Gaussian probability distribution of local bandgaps around a mean bandgap to describe the absorptance[20] and PL spectra.[21] On the other hand, EFs were included in a general sub-bandgap absorption model that uses exponential decays to describe band tails.[19] Other works have described EF also with a Gaussian[6] in order to quantify its impact on the performance of a solar cell. Even though the models for BGF and EF part from different physical principles, they both offer plausible fits to PL spectra of CIGS absorber layers. However, each type of fluctuation is treated independently when both are expected to occur concurrently.[6]

These models assume only one PL emission peak, which is the case of CIGS at room temperature, corresponding to the band-to-band transition.[7] Several peaks might hint to the presence of a secondary phase[22] or deep defects[23] but can also be attributed to interference.[24,25] In the latter, the resulting fringes can be predicted and corrected for with an interference function (IF).[24]

The purpose of this study is to introduce the Unified Potential Fluctuation (UPF) model, which merges the effect of bandgap fluctuations and electrostatic fluctuations to describe non-ideal absorption of a semiconductor. The effect on the band structure can be seen in Fig. 1(c). Using this model, valuable information on potential fluctuations of the absorber layer can be obtained even before integrating it into a solar cell. The presence of these potential fluctuations is evaluated from room temperature PL measurements, which can be directly related to the absorption profile. The model is used to describe the PL spectra of three ultrathin CIGS absorber layers: one without a bandgap gradient (single-stage co-evaporated), one with a notch bandgap profile (three-stage co-evaporated), and a final single-stage co-evaporated one where interference effects were visible. In the latter, a correction with the

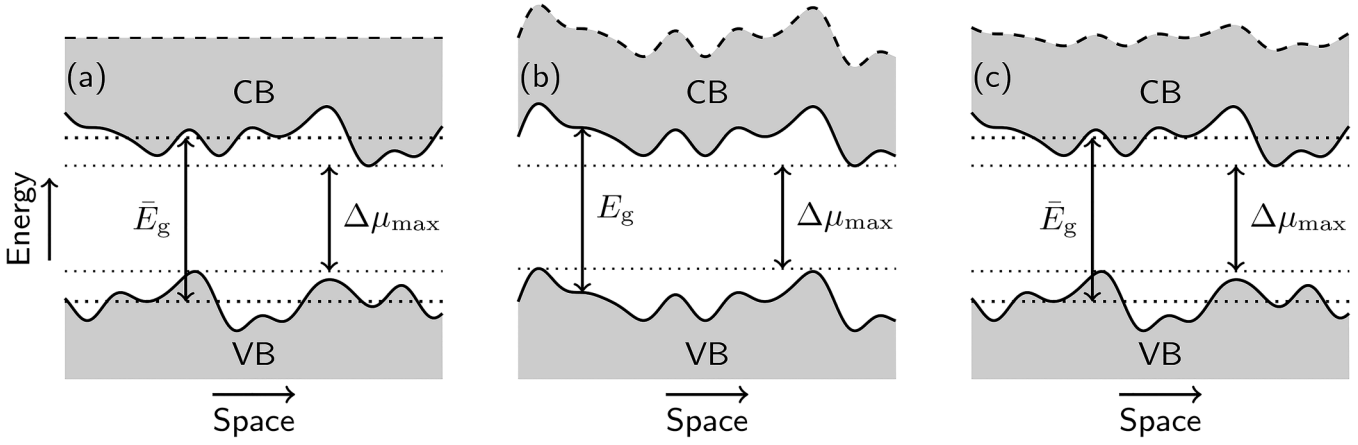

FIG. 1. Schematics of the spatial variation of the conduction band (CB), the valence band (VB), and the vacuum level (top dashed line) in the case of (a) bandgap fluctuations, (b) electrostatic fluctuations, and (c) both bandgap and electrostatic fluctuations.

IF is done. This work starts by elaborating on the existing models for the description of different potential fluctuations and deriving the unified approach, along with the experimental methods used in this study. The models are then applied to experimental PL data, where a possible correction for interference is also considered. Finally, we summarize the most important conclusions and provide a information developed program.

II. MODELING

A. Bandgap fluctuation model

Bandgap fluctuations describe the spatial variations of the fundamental bandgap.[21] Independent variations of the conduction and valence band level across the material result in a spatially inhomogeneous bandgap, as seen in Fig. 1(a). This can have several causes. In CIGS, it is mainly due to a compositional variation (variations in the Ga and In content change the bandgap), stress (strain-induced bandgap variation due to the distortion of the lattice), and stoichiometry (a change in the local Cu content affects the bandgap).[20]

A general model for the influence of BGF on the absorptance was introduced by Rau and Werner.[20] In order to compute the impact of BGF on the efficiency of a solar cell, a probability distribution for the band gap was used. A Gaussian distribution of local bandgaps was assumed around the mean bandgap of the material, expressed as

$$P(E_g^{loc}) = \frac{1}{\sigma_g\sqrt{2\pi}} \exp\left[\frac{-(E_g^{loc} - \bar{E}_g)^2}{2\sigma_g^2}\right], \tag{2}$$

where E_g^{loc} is the local bandgap, $\bar{E}_g$ the mean bandgap, and σ_g the standard deviation of the distribution.[20] Moreover, the absorptance for a given local bandgap is taken as $a(E) = 1$ for $E \geq E_g^{loc}$ and $a(E) = 0$ for $E < E_g^{loc}$. After integration over the spectrum of possible local bandgaps with Eq. (2), the absorptance on a larger scale can be described by

$$a(E) = \frac{1}{2}\,\mathrm{erfc}\left(\frac{\bar{E}_g - E}{\sqrt{2}\sigma_g}\right), \tag{3}$$

where erfc is the complementary error function. Figure 2(a) shows the absorptance for different standard deviations of the Gaussian distribution. As σ_g is increased, the absorptance is symmetrically broadened around $\bar{E}_g$, which creates an absorption tail below the mean bandgap and a gap above. This can be visualized on a logarithmic scale in Fig. 7(a) in Appendix A. The impact of BGF on PL spectra was further developed by Mattheis *et al.*[21] To this end, Eq. (1) is used to describe the *local* PL emission, where the bandgap E_g^{loc} is well defined. Variations in the quasi-Fermi level are possible, which is why this variable is also only locally defined: $\Delta\mu^{loc}$. To quantify the scale of the fluctuations in comparison with the charge carrier transport, a parameter $\beta \in [0, 1]$ is introduced.[21] For variations occurring on small length scales ($\beta = 0$), the quasi-Fermi levels flatten and $\Delta\mu^{loc}$ is constant. For large scale fluctuations ($\beta = 1$), charge carrier transport can be neglected and the quasi-Fermi levels follow the local bandgap. To account for all fluctuation length scales, the authors define $\Delta\mu^{loc} = \mu_0 + \beta E_g^{loc}$,[21] with $\mu_0 \in \mathbb{R}$ being a constant.

Using the Boltzmann approximation for the exponent in Eq. (1) (valid for $E - \Delta\mu^{loc} \gg k_B T$), the local contributions to the PL emission can be integrated with the Gaussian probability distribution to obtain the *global* PL emission,

$$\phi_{PL}(E) = \frac{\pi}{h^3c^2} E^2 \mathrm{erfc}\left(\frac{\bar{E}_g - E + \beta\sigma_g^2/(k_B T)}{\sqrt{2}\sigma_g}\right) \times \exp\left[-\frac{E - \mu_0 - \beta\bar{E}_g}{k_B T} + \frac{1}{2}\left(\frac{\beta\sigma_g}{k_B T}\right)^2\right]. \tag{4}$$

Figure 2(b) shows how the area-normalized PL emission is affected by σ_g in the case of small and large scale fluctuations ($\beta = 0$ and $\beta = 1$, respectively). In general, it is observed that the PL peak broadens for larger fluctuations, which can be expected when considering the effect on the absorptance in Fig. 2(a). For large scale fluctuations, the peak is centered around the mean bandgap of 1 eV. This peak is shifted toward lower energies for smaller scale fluctuations, and this phenomenon is intensified as σ_g increases. This is why the continuous and dashed green lines overlap in Fig. 2(b). These area-normalized spectra are independent of μ_0, as this is just a scaling factor in Eq. (4).

B. Tail model

Changes in the potential also arise from *electrostatic fluctuations*, which distorts the band structure of the material.[7] In this case, the valence and conduction band are shifted together while keeping a constant bandgap, as seen in Fig. 1(b). This is a consequence of the distribution of charged states, originating from structural defects, doping atoms, and impurities.[6] In these disordered materials, states within the average bandgap are introduced to form the so-called band tails, which extend the absorption to energies below the bandgap.

Typical functional forms for these band tails are exponential decays from the edge of the bandgap into the forbidden gap, typically called Urbach tails.[26] Shklovskii and Efros[27] noted a sharper decay for tails arising from charged defects, which results in an exponential decay to the power of 1.25. Furthermore, a 1.5 power exponentially decaying absorption tail was identified by Franz[28] and Keldysh[29] when an electric field is present, possibly caused by charged impurities. As CIGS has a high degree of compensation and charged grain boundaries,[4] exponential powers near 1.25 and 1.5 can be expected instead of Urbach tails with a power of 1.

Generally, the functional forms of density of states G of the tail states are described as exponentials, which Katahara and Hillhouse[19] bundled into an exponential function for energies below the bandgap,

$$G(\Delta E) = \exp\left(-\left|\frac{\Delta E}{\gamma}\right|^{\theta}\right) \quad (E < E_g), \tag{5}$$

where γ and θ are the characteristic energy and power of the decay,

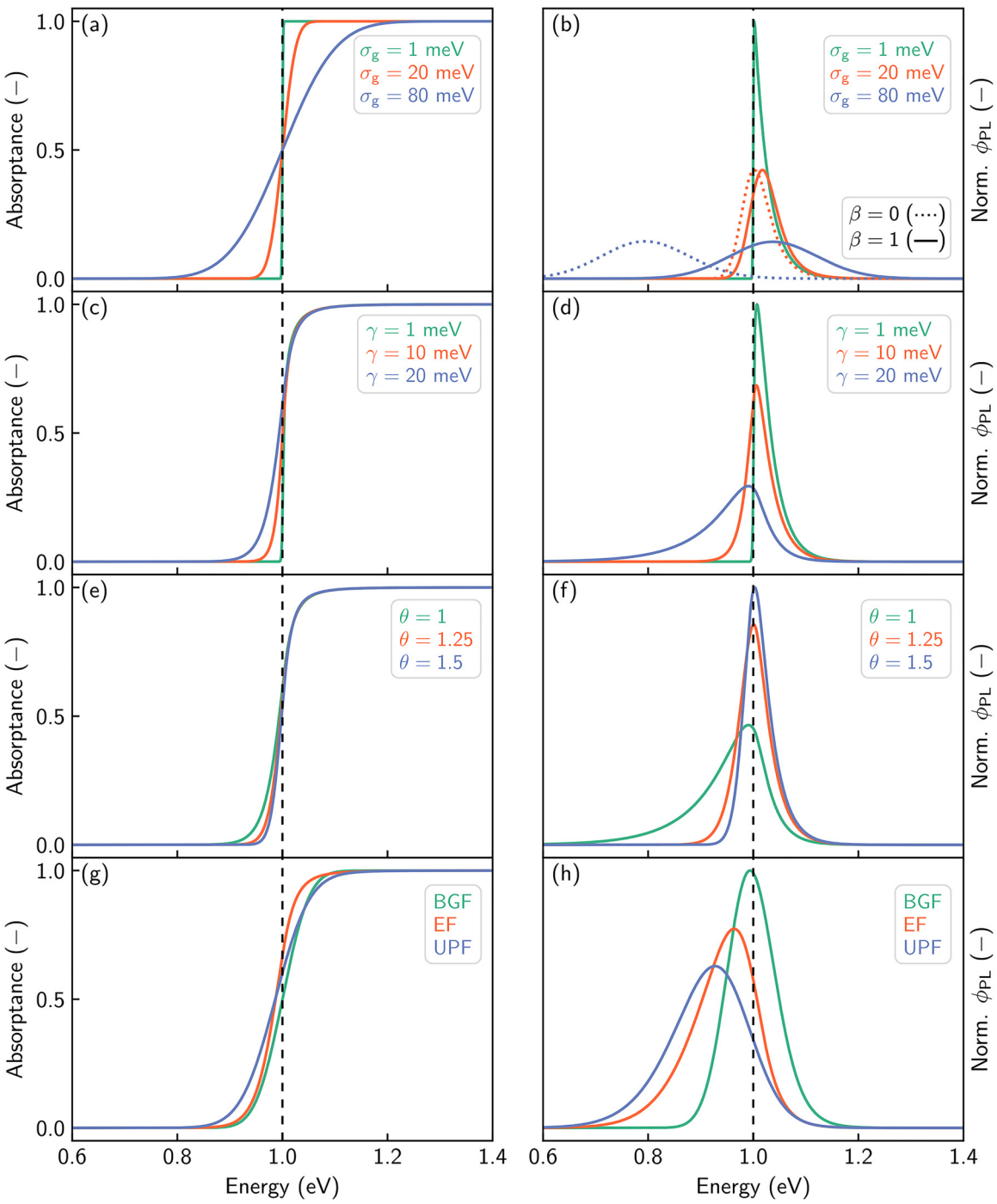

FIG. 2. Absorptance (left column) and area-normalized PL spectra (right column) for different model parameters in the BGF, EF, and UPF models. (a) and (b) BGF model for $\sigma_g \in \{1, 20, 80\}$ meV and $\beta \in \{0, 1\}$. The absorptance profile is not affected by the length scale of the fluctuations. (c) and (d) EF model for $\gamma \in \{1, 10, 20\}$ meV and $\theta = 1$. (e) and (f) EF model for $\theta \in \{1, 1.25, 1.5\}$ and $\gamma = 20$ meV. (g) and (h) BGF, EF, and UPF models for $\sigma_g = 40$ meV, $\beta = 0.5$ (intermediate scale fluctuations), $\theta = 1.25$, and $\gamma = 35$ meV. For all subplots, it holds (where applicable): $\bar{E}_g = E_g = 1$ eV, $T = 300$ K, and $a_0 d = 15$, as suggested in Katahara *et al.*[19] The dashed line is plotted at the (average) bandgap.

respectively, and $\Delta E = E - E_g$.[30] To construct the density of states for all energies, this behavior under the bandgap was joined with an ideal square root behavior of the density of states above the band, typical for direct semiconductor materials.[31] This is done by means of a convolution operation, expressed as

$$G(\Delta E) = \frac{1}{2\gamma\Gamma(1+1/\theta)} \int_{-\infty}^{\Delta E} \exp\left(-\left|\frac{\Delta E_*}{\gamma}\right|^{\theta}\right) \times \sqrt{\Delta E - \Delta E_*}\, \mathrm{d}\Delta E_*, \tag{6}$$

where Γ is the gamma function.[30] The prefactor of the integral is included for normalization purposes. Based on this density of states, the absorption coefficient α can be computed with $\alpha(E) = \alpha_0 G(E)$, where α_0 is a proportionality parameter dependent on the material. The absorptance is then given by

$$a(E) = 1 - \exp[-\alpha(E)d], \tag{7}$$

where d is the characteristic length over which carriers are generated and recombined.[19] The behavior of the absorptance when varying the values of γ and θ is shown in Figs. 2(c) and 2(e). As γ increases, the tail states penetrate more into the bandgap, which broadens the absorptance toward lower energies. For a change in θ, the increase of the exponential power of decay results in a reduction of the tail states. In both cases, the effect on energies above the bandgap is minimal. Again, Figs. 7(b) and 7(c) in Appendix A plot these absorptances on a logarithmic scale, allowing for a better visualization of the tail states. Finally, the PL spectrum is computed with Eq. (1), to which an occupation dependent factor is subsequently added,[19]

$$\phi_{\mathrm{PL}}(E) = \frac{2\pi}{h^3c^2} \frac{E^2}{\exp\left(\frac{E-\Delta\mu}{k_{\mathrm{B}}T}\right) - 1} \times \left\{1 - \exp\left[-G(\Delta E)\alpha_0 d\left(1 - \frac{2}{\exp\left(\frac{E-\Delta\mu}{2k_{\mathrm{B}}T}\right) + 1}\right)\right]\right\}. \tag{8}$$

The resulting area-normalized PL spectra for different values of γ and θ are shown in Figs. 2(d) and 2(f). In all cases, a broader absorptance results in the widening of the PL peak. Both parameters have an impact on the energy at which the emission peaks such that a significant presence of tail states results in a peak shift toward lower energies, as can be expected. The impact of changing $\Delta\mu$ is negligible when considering normalized spectra. Given that electrostatic fluctuations give rise to band tails in CIGS absorber layers, this model will be called the EF model in the remainder of this study.

C. Unified potential fluctuation model

The previous paragraphs introduced two existing models for non-ideal absorptance in semiconductors. The physical motivation behind these two models is the possibility of compositional variations in the material (which can change the local bandgap) and the random distribution of charged defects (which influences the local electrostatic potential), both of which can cause fluctuations of the potential landscape. In reality, one can expect both effects to take place simultaneously,[6] as was introduced in Fig. 1(c). Here, independent variations of the conduction and valence band edge are superimposed to a varying vacuum level.

Rey *et al.*[32] already considered the joint contribution of bandgap and electrostatic fluctuations in the absorption of kesterites. There, a Gaussian distribution of bandgaps was combined with an Urbach exponential tail. In this study, we introduce a more generalized approach, parting from the BGF model (also a Gaussian distribution) and EF model (power exponential function convoluted with a square root) introduced earlier. In this way, we combine bandgap and electrostatic fluctuations to form the *unified potential fluctuations* model for which the impact on the absorptance properties and PL emission is considered. Starting from the general expression for the *global* absorptance a^{glob} in the BGF model, we have[21]

$$a^{\mathrm{glob}}(E) = \int_{-\infty}^{\infty} a^{\mathrm{loc}}(E, E_{\mathrm{g}}^{\mathrm{loc}}) P(E_{\mathrm{g}}^{\mathrm{loc}})\, \mathrm{d}E_g^{\mathrm{loc}}. \tag{9}$$

In the BGF model, $a^{\mathrm{loc}}(E, E_{\mathrm{g}}^{\mathrm{loc}})$ is then assumed to be a step function for each local bandgap. For the UPF model, we choose to include an absorptance term as described in the EF model, parting from the ideal semiconductor behavior to include a decaying tail at $E_{\mathrm{g}}^{\mathrm{loc}}$ in the absorptance spectrum. In this sense, $a^{\mathrm{loc}}(E, E_{\mathrm{g}}^{\mathrm{loc}})$ is defined by Eq. (7), redefining ΔE as $\Delta E^{\mathrm{loc}} = E - E_g^{\mathrm{loc}}$ in Eq. (6). This approach allows for the simultaneous occurrence of a fluctuating local bandgap and the presence of tail states as a consequence of charged defects. Combining all the expressions, we obtain

$$a^{\mathrm{glob}}(E) = \int_{-\infty}^{\infty} \left\{1 - \exp[-G(\Delta E^{\mathrm{loc}})\alpha_0 d]\right\} \times P(E_{\mathrm{g}}^{\mathrm{loc}})\, \mathrm{d}E_g^{\mathrm{loc}}, \tag{10}$$

where $P(E_{\mathrm{g}}^{\mathrm{loc}})$ and $G(\Delta E^{\mathrm{loc}})$ are defined by Eqs. (2) and (6), respectively. For the analysis of PL spectra, the derivation is similar to the procedure followed for the absorptance. The general expression for the global absorptance in the BGF model is[21]

$$\phi_{\mathrm{PL}}(E) = \frac{2\pi}{h^3c^2} \int_{-\infty}^{\infty} E^2 \exp\left[-\frac{E - (\mu_0 + \beta E_{\mathrm{g}}^{\mathrm{loc}})}{k_{\mathrm{B}}T}\right] \times a^{\mathrm{loc}}(E, E_{\mathrm{g}}^{\mathrm{loc}}) P(E_{\mathrm{g}}^{\mathrm{loc}})\, \mathrm{d}E_g^{\mathrm{loc}}, \tag{11}$$

assuming a Boltzmann approximation. Again, we can assume a local absorption profile as in the EF model to arrive at

$$\phi_{\mathrm{PL}}(E) = \frac{2\pi}{h^3c^2} \int_{-\infty}^{\infty} E^2 \exp\left[-\frac{E - (\mu_0 + \beta E_{\mathrm{g}}^{\mathrm{loc}})}{k_{\mathrm{B}}T}\right] \times \left\{1 - \exp[-G(\Delta E^{\mathrm{loc}})\alpha_0 d]\right\} \times P(E_{\mathrm{g}}^{\mathrm{loc}})\, \mathrm{d}E_g^{\mathrm{loc}}. \tag{12}$$

The UPF model quantifies potential fluctuations in terms of BGF (with $\bar{E}_g$, σ_g, and β) and EF (with γ and θ). Moreover, the temperature T and the product $\alpha_0 d$ in the absorptance terms in Eqs. (10) and (12) are left as free parameters of the model. Figure 2(g) plots the absorptance of the three models for a reference set of parameters, with Fig. 7(d) in Appendix A on a logarithmic scale. Parting from the symmetrical BGF model for the absorptance around the bandgap of 1 eV, the symmetry is broken when looking at the UPF model, given the inclusion of non-ideal absorptance from the EF. The absorptance of the energies below the bandgap is increased as a consequence of the tail states that are now present. Above the bandgap, it is clear that the EF model for absorptance deviates somewhat from the ideal case, which is a consequence of the square-root density of states in the convolution operation in Eq. (6). This causes the UPF absorptance model to drop below the BGF one, which assumed a unity absorptance above the local bandgap. In Fig. 2(h), the area-normalized PL intensities for each model are shown, which depicts what can be expected based on the absorptance in Fig. 2(g). The UPF model presents the broadest absorptance for the same parameters as in the BGF and EF models, which results in the broadest PL emission. The emission peaks of the BGF and EF models are around the same energy, and the combination of these two in the UPF model noticeably shifts the peak to a lower energy. Again, the impact of μ_0 and $\Delta\mu$ is neglected on these normalized spectra.

III. EXPERIMENTAL

Three CIGS absorber layers, denoted samples 1, 2, and 3, are used to evaluate the models presented in Sec. II. All the samples were prepared by either single- or three-stage co-evaporation process on soda lime glass/Mo substrates at 550 °C and have a thickness of around 500 nm. XRF measurements revealed that $[Cu]/([Ga]+[In]) = CGI \approx 0.8$ and $[Ga]/([Ga]+[In]) = GGI \approx 0.3$ for all absorber layers. Single-stage sample 1 was deposited on a Mo/6 nm Al_2O_3/5 nm NaF stack. The holes that are formed in the Al_2O_3 back layer enhance light scattering, which reduces the interference of light reflecting back into the absorber layer.[33] Moreover, the front surface was passivated with Al_2O_3 to increase the PL yield. Sample 2 was deposited through a three-stage process and underwent a post-deposition treatment (PDT) with RbF, similar as the KF treatment presented by de Wild *et al.*[13] The stack is finalized with a 30 nm CdS front layer grown by means of chemical bath deposition. The roughness of the three-stage absorber layer and the PDT are believed to limit the occurrence of interference. Finally, sample 3 was deposited with a single-stage process, with a front CdS layer grown through chemical bath deposition. The PL measurements of this sample showed interference, which allowed the study of a correction with the interference function for a laser power series measurement.

Regarding the PL data acquisition, two different setups were used. The spectrum gathered for sample 1 is from a photospectrometer from PicoQuant with a TimeHarp 260 single photon counter for the time resolved measurements. The laser excitation wavelength was 532 nm at an approximate intensity of 0.1 W cm^{-2} and a repetition rate of 3 MHz. For the intensity dependent measurement of sample 3, a Hamamatsu spectrometer was used. The excitation wavelength is unchanged at 532 nm, now with a 15 kHz rate. This setup allowed for a variation of the laser intensity from 1 to 46 mW. Finally, the data for sample 2 were also measured with this setup at a fixed power of 3 mW. All PL spectra are corrected for the optical path and instrumental response. No absolute intensity calibrations were possible given the unavailability of a reference light source to calibrate the setup. Therefore, all the analyses in this work were done on normalized PL spectra, which still allowed for the study of the peak widths as a consequence of potential fluctuations.

IV. RESULTS AND DISCUSSION

The BGF, EF, and UPF models introduced in Sec. II were implemented in Python, followed by the development of a user-friendly interface that incorporates the models into one program. More details on the program are explained in Appendix B 1, and the code can be accessed under Appendix B 2. The program is used to fit experimental PL spectra of samples 1 and 2 to compare the different absorptance models in Sec. IV A. In Sec. IV B, the PL spectra of sample 3, where interference fringes are present, is touched upon. As explained in Sec. III, only normalized data are used.

A. Modeling of experimental data

The specifics of the preparation of samples 1 and 2 allowed for an interference-free PL measurement such that the PL models can be applied directly. To start, fits of the PL spectrum of sample 1 were done with the BGF, EF, and UPF models with relaxed limits in the parameter space of the fitting routine: $E_g \in [1, 1.4]$ eV, $\sigma \in [1, 100]$ meV, $\gamma \in [1, 100]$ meV, $\theta \in [1, 2]$, and $T \in [250, 350]$ K, with $\alpha_0 d$ fixed at 15, as suggested by Katahara and Hillhouse.[19] Moreover, μ_0 and $\Delta\mu$ are excluded from the analysis: the former because it does not affect normalized PL spectra and the latter because of its negligible impact after normalization. Table I summarizes the fitted parameters worthy of consideration, along with the average fit error ε as defined in Eq. (B1).

The errors indicate that decent fits are obtained for all models, the UPF model yielding the best results. Given the GGI ratio ($[Ga]/([Ga]+[In])$) of 0.3 for this sample, we can expect a bandgap of around 1.20 eV,[34] which is below the values found for all the fitted models. This has to do with the definition of the bandgap in each case. Experimentally, the high slope of the absorption coefficient tail is extrapolated, and the value of the bandgap is read off the intercept on the energy axis in the form of Tauc plots.[35] This results in bandgaps lower than the definition in the BGF case, for instance, where the *average* band gap is used and is located halfway the absorptance tail. Note how, in the absorptance

TABLE I. Subset of the fitted parameters of the BGF, EF, and UPF models for the PL spectrum of sample 1 in the case of relaxed parameter bounds along with the model errors.

Model	E_g (eV)	θ	T (K)	ε
BGF	1.24	⋯	250	0.0160
EF	1.28	1.82	350	0.0083
UPF	1.24	1.00	350	0.0067

plots of Fig. 2(a), the average bandgap is the same for the three cases, even though different bandgaps can be expected as σ_g changes. Moreover, the bandgap in the EF model is defined very close to the tail start [see Figs. 2(c) and 2(e)] and is independent of the choice of γ and θ. In the BGF and UPF models, the parameter β also introduces some freedom in the choice of the average bandgap when fitting normalized PL spectra, as changing this parameter merely results in an energy shift. For these reasons, a direct comparison between bandgaps of the models and experimentally determined values is not possible without prior analysis.

It is worth noting that fits of the EF model often yield very high temperatures, beyond what has been measured externally.[11] This was also the case here, where the fitted temperature reached the upper bound of 350 K in the program. This issue also seems to be inherited by the UPF model, also reaching the maximum temperature in the fit. On the other hand, the fitted temperature in the BGF model reaches the lower bound of the program: 250 K. We do not expect a large increase in the temperature during the measurement and certainly no decrease with respect to room temperature. Therefore, the fitted temperatures of all models appear to be unreliable for this normalized PL spectrum. Moreover, the exponential tail parameter θ also reached unanticipated values. Electrostatic fluctuations in CIGS are thought to be caused by the random distribution of charged states,[4] which indicates that $\theta \in [1.25, 1.5]$.[19] Both the fit values of the EF and UPF models are outside this range. It is clear how the freedom given to θ and T in the parameter space resulted in unexpected values. As more variables are added to a model, we might compromise its ability to discern the influence of parameters on the fit, which is particularly important for the many variables in the UPF model. A solution is, therefore, to fix as many parameters as known beforehand and limit the parameter ranges to physically feasible values. Fixing the bandgap is not desirable, as mentioned earlier, but a sample temperature near room temperature (293 K) and $\theta \in [1.25, 1.5]$ are fair assumptions. Under these new conditions, the models were once again fitted to the data. The fits and relevant fit parameters are presented in Fig. 3(a), where the PL spectrum and two more shifted versions are shown to visualize the quality of the fit for each model. It is evident how the UPF model provides, once again, a better fit to the data. For this model, the error shown in the lower pane of Fig. 3(a) is the closest to 0. The BGF model correctly approaches the slope of the data in the high-energy tail of the peak but fails to do so in the lower energy range. This is the opposite for the EF model. By superimposing these two in the UPF model, both sides of the peak are accurately matched. The average fit errors have logically increased and now correspond to 0.0169, 0.0207, and 0.0076 for the BGF, EF, and UPF models, respectively. The quality of the EF fit suffers the most from the restriction of the parameter space, evidencing the difficulty of this model to adapt to the measurement data under modest assumptions. It is clear how the UPF model combines both types of fluctuations, bandgap and electrostatic, to arrive at a closer match to the data. The BGF model widens the peak by including bandgap fluctuations with a standard deviation of 53 meV, whereas the EF model incorporates an exponential decay with a characteristic energy of 48 meV and a power of 1.5. All these values are reduced in the UPF model since it combines

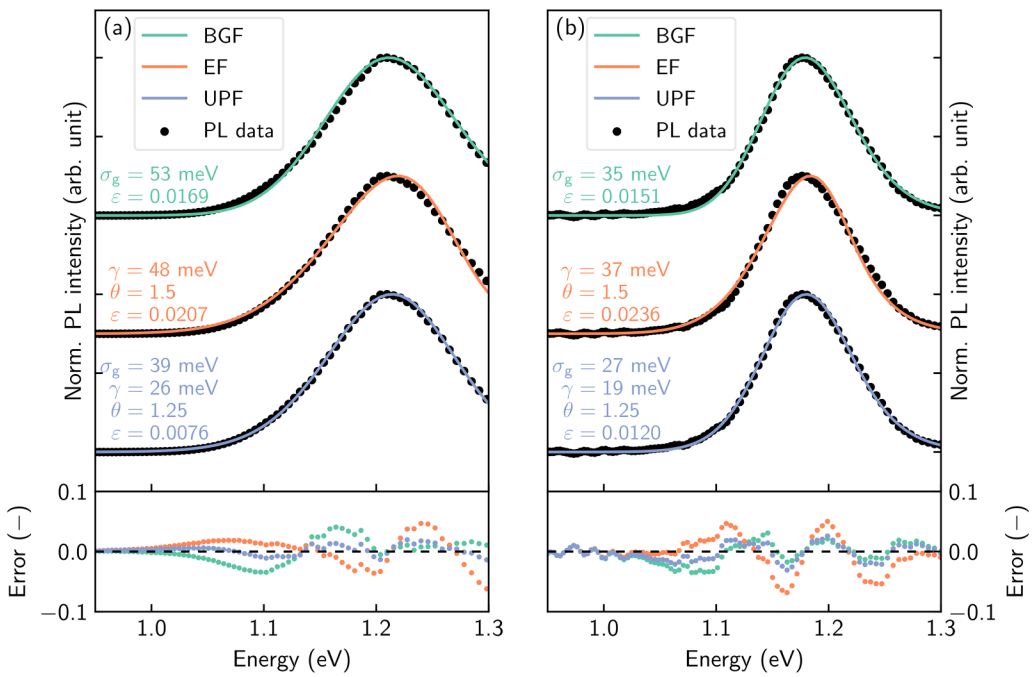

FIG. 3. Normalized PL spectrum along with two shifted copies of (a) sample 1 and (b) sample 2, fitted with the BGF, EF, and UPF models with a limited parameter space: $T = 293$ K and $\theta \in [1.25, 1.5]$. The lower panes plot the difference between the data and the models.

the impact both potential fluctuations have on the peak width, offering a superior fit even with a constricted parameter space. Logarithmic plots of these fits, shown in Fig. 8(a) in Appendix A, evidence that the very deep tails in the PL spectrum are not followed by the models properly anymore. This has to do with the full spectrum fitting routine used in this study, which not only focuses on the tails but on the complete PL peak.

For some analyzed CIGS samples, the improvement with the UPF model is less evident, as is the case for sample 2. Figure 3(b) plots the PL data and model fits for this sample, in the same way as Fig. 3(a) did for sample 1. Once again, we restrict ourselves to $T = 293\,\mathrm{K}$ and $\theta \in [1.25, 1.5]$. The BGF model seems to correctly match the width of the PL spectrum but once again fails to approximate the luminescence at the lower end of the peak (between 1.05 and 1.1 eV), i.e., where sub-bandgap emission takes place. This region is, in turn, slightly overestimated by the EF model, and an overall mismatch with the data is found for this model. Given that sample 2 was co-evaporated in a three-stage process, there are intrinsic bandgap variations in the depth of the sample given a Ga gradient. This can explain the dominance of BGF over EF and the resulting fit errors for each model. The UPF model again provides the closest match to the data, but the improvement from the BGF model is minimal, mainly improving the lower tail of the peak [as seen in the lower pane of Fig. 3(b)]. If we were to consider these fits on a logarithmic scale [Fig. 8(b)], it is clear that the deep tails are better described by the EF model. Once again, the fits performed are based on the full spectrum of the PL peak, which may result in these discrepancies when considering only the tails.

B. Interference correction

When analyzing PL spectra, it is important to distinguish between actual PL emission and optical artifacts of the measurement, such as interference. This causes the appearance of additional peaks in the PL spectra or significant shoulders,[25] which makes the analysis of potential fluctuations rather cumbersome. Figure 4(a) depicts this effect for a series of measurements of sample 3 at different laser excitation intensities. The dots represent the measurement data and the lines the best fit according to the UPF model.

Depending on the sample, several peaks might actually hint to the presence of a secondary phase in the material, as can happen in CZTSe.[22] However, it can also lead to the incorrect interpretation of peaks as multiple phases.[36,37] Previous characterizations with GDOES and XRD on similar single-stage layers as in Fig. 4(a) excluded this possibility.[13] Moreover, the thermal quenching of possible defect states at room temperature makes defect-related transitions improbable given the small activation energy it would have based on the shown plot. We can, therefore, assume that the PL emission comes from band-to-band transitions[7] such that interference offers a plausible explanation for the distortion of the spectra.

From the fitted UPF models in Fig. 4(a), it is visible how no proper description of the data is possible. The BGF and EF model fits were also not satisfactory (not shown here). Interference effects can be corrected for from an experimental or a modeling approach. Previous studies explore the possibility of averaging PL spectra over several excitation angles[25] or including a scattering layer to reduce coherent superposition of light.[38] Larsen *et al.*[24] conducted a comprehensive

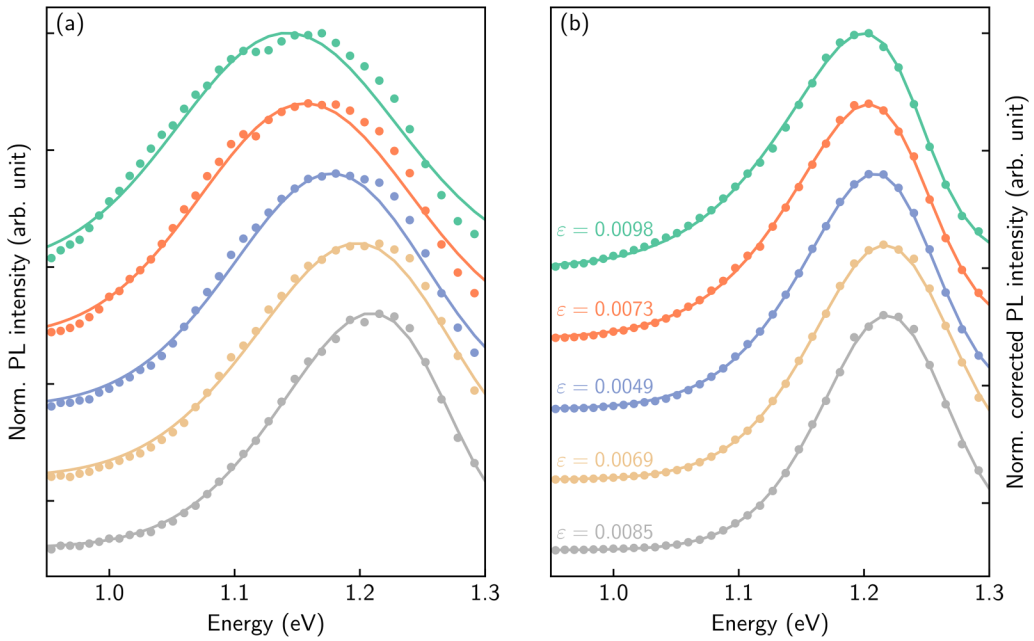

FIG. 4. (a) Normalized PL spectra measured at different laser excitation intensities and (b) normalized PL spectra after interference correction with $L(z) = \delta(z - 363\,\mathrm{nm})$ of sample 3. In both subplots, the dots represent the measurement data and the line the best fit based on the UPF model. A fixed bandgap of 1.24 eV was chosen for (b). Laser intensity in mW from top to bottom: 1 (green), 3 (orange), 10 (purple), 30 (gold), and 46 (gray).

study on interference corrections for CIGS thin films. Here, we implement an interference correction by means of an interference function (IF) model and suggest how its estimation can be improved with a laser power series as the one shown in Fig. 4(a).

The IF was first derived by Holm *et al.*,[39] and it is based on the prediction of the interference fringes in a stack of thin-film layers. It includes both the effect of multiple-beam interference (caused by multiple reflections of the PL emission at the interfaces of the material, as typically seen in transmission measurements) and wide-angle interference (caused by the interference of the directly emitted beam and the one reflected at the bottom interface).[24] The model starts by assuming the configuration shown in Fig. 5, typical for CIGS absorber layers. The complex coefficient of each layer can be written as $N_x = n_x + ik_x$, $x \in \{1, 2, 3\}$ from which Fresnel's coefficients for reflection (r_{xy}) and transmission (t_{xy}) for light traveling from any layer x–y can be computed. These coefficients were adapted to account for the interface roughness, as described by Larsen *et al.*[24] Next, it is assumed that the spontaneous emission is caused by randomly oriented dipoles, and the contribution over the full sphere solid angle is averaged.[39] This results in the quantification of the emission probabilities for each light polarization. If we assume perpendicular light incidence ($\theta_1 = 0$ such that $\theta_2 = 0$), we obtain[24]

$$P(\lambda, z) = \frac{1}{8\pi}\frac{n_2}{n_1}|t_{21}|^2\frac{|1 + r_{23}\exp(i\delta)|^2}{|1 - r_{21}r_{23}\exp(i\phi)|^2}, \tag{13}$$

where $\phi = 4\pi N_2 d/\lambda$ and $\delta = 4\pi N_2(d - z)/\lambda$. All in all, the resulting interference function IF is computed as the integration of this emission probability $P(\lambda, z)$, the excitation intensity $E(z)$, and the luminescence distribution $L(z)$ over the depth of the sample,

$$\mathrm{IF}(\lambda) = \frac{\int_0^d P(\lambda, z)L(z)E(z)\,\mathrm{d}z}{\int_0^d L(z)E(z)\,\mathrm{d}z}. \tag{14}$$

Typically, $E(z) = A\exp(-\alpha_{\mathrm{laser}}z)$, where α_{laser} is the absorption coefficient at the laser wavelength, following Lambert–Beer's law. $L(z)$ quantifies the emission profile, which is not straightforward to predict, since it is dependent on the absorber layer emission characteristics. A uniform emission throughout the depth of the sample indicates that $L(z) = 1$, whereas more localized emissions can be approximated with Gaussians centered at the emission depth.[24] After computing the interference function, the corrected PL emission spectrum can be simply found with $\phi_{\mathrm{PL}}^{\mathrm{corr}} = \phi_{\mathrm{PL}}/\mathrm{IF}$.

Following the emission profile $L(z)$ used by de Wild *et al.*,[40] we will correct for interference by using a Dirac delta function, which removed the fringe distortion from the measurements. As in that study, the CdS layer is omitted due to the proximity of its refractive index to that of CIGS in the investigated spectral range and the fact that no sharp interface is expected.[40] Moreover, an rms roughness of around 50 nm was measured and used to account for scattering in Fresnel's equations.[24] Figure 4(b) plots the same PL spectra as in Fig. 4(a), this time with an interference correction using an IF with $L(z) = \delta(z - 363\,\mathrm{nm})$. The choice for an emission profile at this depth is based on the minimization of the addition of the UPF fit errors for the plotted laser intensities. This gave a total added error of 0.0374. It is also visually evident how this choice of IF removes the broad peak shoulders evident in Fig. 4(a).

When looking at only one PL spectra, it might be the case that several $L(z)$ allow for a proper interference correction. This is the case for the measurement at 46 mW, where by using $L(z) = \delta(z - 195\,\mathrm{nm})$, the peak distortion was removed and the UPF model could be fitted with great accuracy, as seen in the bottom curve of Fig. 6. Given that the measurements are done at the same spot, it is reasonable to assume the IF to remain unchanged for other excitation intensities since the material properties that define the function stay the same. If we were to use $L(z) = \delta(z - 195\,\mathrm{nm})$ to correct for the measurement at 1 mW, for instance, an unsatisfactory fit with the UPF model is obtained. This points to the fact that this choice of $L(z)$ is not suitable for the

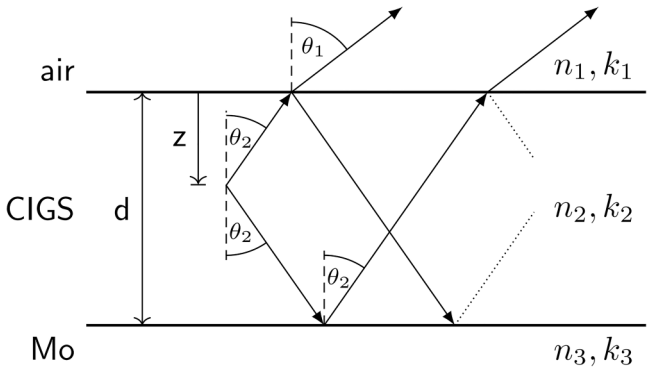

FIG. 5. Visualization of assumed stack of layers and the relevant parameters for the computation of the IF. Inspired by Larsen *et al.*[24]

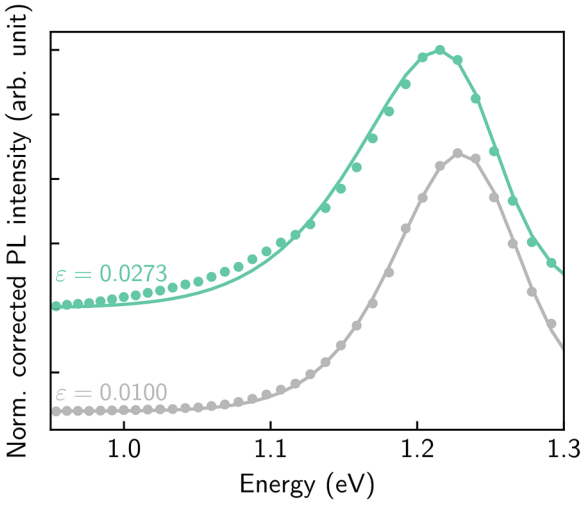

FIG. 6. Normalized PL spectra after interference correction with $L(z) = \delta(z - 195\,\mathrm{nm})$ at laser excitation intensities of 1 mW (top, green) and 46 mW (bottom, gray) of sample 3. The dots represent the measurement data and the line the best fit based on the UPF model.

sample in general despite the encouraging fit from correcting only the 46 mW measurement.

By means of this example, we encourage the use of several PL measurements at different laser excitation intensities when the interference function is to be used to remove fringes. Under the assumption that the IF is unaffected from one measurement to the other, it allows for a better selection of the emission profile $L(z)$ given the possibility of discarding profiles that are not able to adequately correct all measurements simultaneously.

V. CONCLUSION

In conclusion, a unified model for potential fluctuation (UPF) was formulated based on existing models for bandgap and electrostatic fluctuations (BGF and EF, respectively). The models were fit to measured PL spectra of both ultrathin single- and three-stage co-evaporated CIGS samples, and the results show a much better fit for the UPF model compared to the BGF and EF models. The UPF introduces a new model that takes into consideration both sources of potential fluctuations, providing a more complete description of the physical phenomena involved in the absorption and consecutive emission of light involved in PL. The presence of these fluctuations in absorber layers partially explains losses in V_{oc} of the resulting solar cell. Therefore, the fitted model parameters can provide an insight into the extent of these losses as a consequence of deposition conditions, post-deposition treatments, etc., even before integrating the absorber layer into a device. The application of this model is not limited to only CIGS layers, but could be generally applied to direct bandgap semiconductors. However, careful consideration of the parameter space in the model is needed to ensure realistic fitting outcomes for which previous knowledge of the nature of the fluctuations can be useful. Moreover, the use of absolute PL spectra could increase the parameter sensitivity of the model. An extension to the analysis presented in this work could include the manufacturing of solar cells from absorber layers analyzed with the UPF model in order to relate the presence of potential fluctuations to the solar cell performance. Some PL spectra were distorted by interference effects for which an interference function (IF) was used to correct for the fringes. It was shown how the correction using several measurements on the same spot under different laser excitation intensities can help to search for the right luminescence distribution needed in the IF.

ACKNOWLEDGMENTS

Dr. J. de Wild and Professor B. Vermang received funding from the European Union's H2020 research and innovation programme under Grant Agreement No. 715027 for this work.

AUTHOR DECLARATIONS

Conflict of Interest

The authors have no conflicts to disclose.

DATA AVAILABILITY

The data that support the findings of this study are available from the corresponding author upon reasonable request.

APPENDIX A: LOGARITHMIC PLOTS

Here, some logarithmic plots of the figures in the main text, worthy of consideration, are presented.

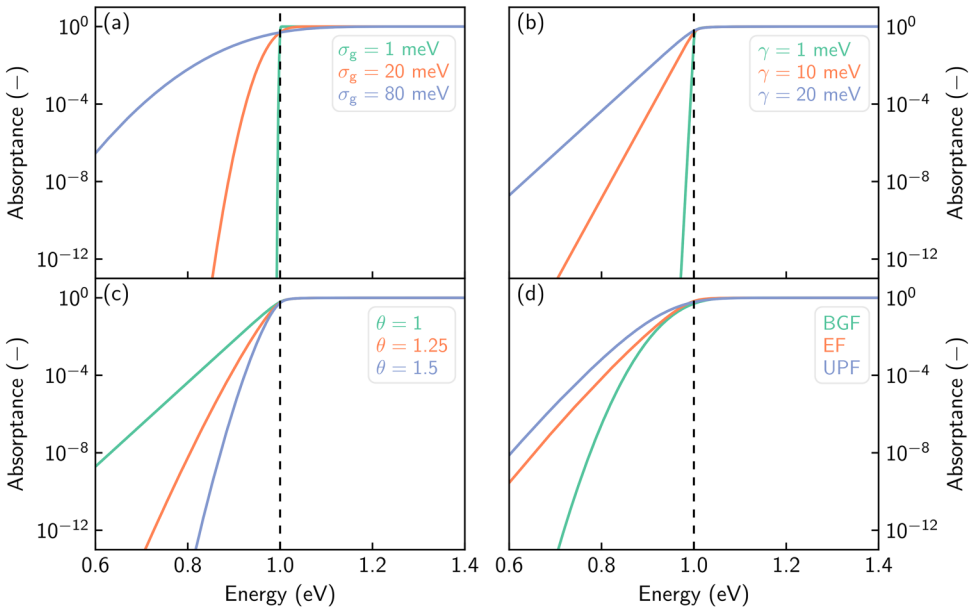

FIG. 7. Logarithmic plots of the absorptance for the same set of parameters as Fig. 2. (a) BGF model for varying σ_g, (b) and (c) EF model for varying γ and θ, respectively, and (d) BGF, EF, and UPF models for the same set of model values.

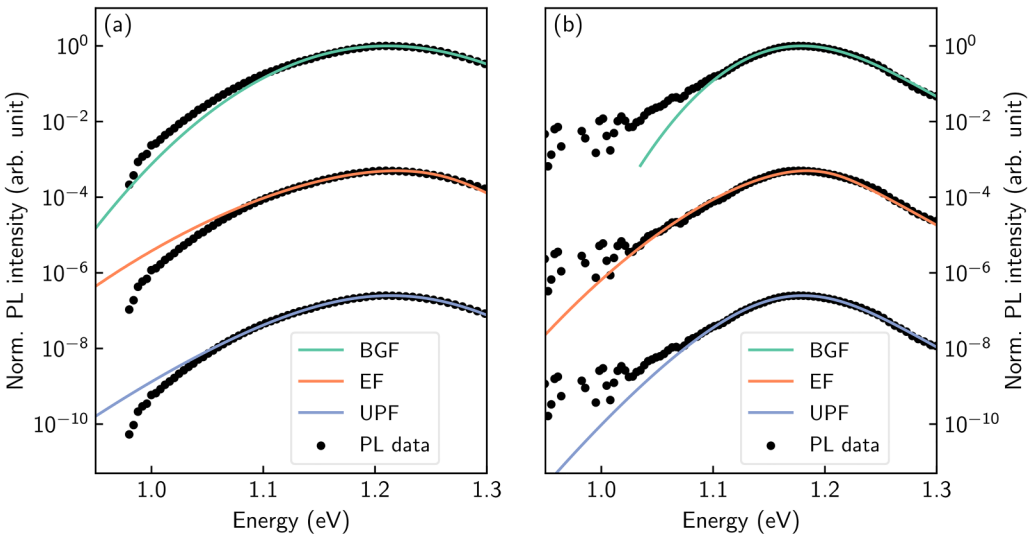

FIG. 8. Logarithmic PL plots of (a) sample 1 and (b) sample 2 for the same fits as Fig. 3.

APPENDIX B: PL MODELING PROGRAM

1. Program description

The PL modeling program, with the possibility of fitting the BGF, EF, and UPF models and correcting for interference with the IF, was fully developed in Python. A graphical user interface based on *Tkinter* was built on top of the modeling back end to expand its accessibility, providing the user with a straightforward fitting tool. In the program, model parameters can be adjusted manually to directly visualize the impact of a variable on the PL spectrum. Here, a quick overview of the methods used in the program is presented. The code and a more in-depth explanation can be found accessed from Appendix B 2.

The parameter bounds of the models can be easily configured by providing an optional configuration file to the program. All the fits are done with the curve_fit tool in scipy.optimize, which is a non-linear least square fitting routine that follows the Trust Region Reflective algorithm. It is wrapped around a function that enables the dynamic variation of the number of parameters to be fitted given the user's choice to fix model parameters. Numerical integrations use the scipy.integrate.quad function, which computes definite integrals based on QUADPACK. To speed up the computation of the EF model, a 2D lookup table was generated for the integral in Eq. (6) for the variables $\Delta E/\gamma$ and θ, as suggested by Katahara and Hillhouse.[30] This also improves the computation time of the UPF model. Here, the final integration step of the model is done with numpy.trapz in the non-zero interval of the integrand, once again improving the computation time. Finally, the average model errors are computed with

$$\varepsilon = \sqrt{\frac{\sum_i \left(I_{\mathrm{PL},i} - I_{\mathrm{PL},i}^{\mathrm{mod}}\right)^2}{N}}, \tag{B1}$$

where $I_{\mathrm{PL},i}$ and $I_{\mathrm{PL},i}^{\mathrm{mod}}$ are the experimental and modeled normalized PL intensity sampled according to the input data, respectively, and N is the number of samples in the measurement.

2. Code availability

The Python program developed for this work, including the source code and a manual, is published in GitHub: https://github.com/erikspaans/PL-Modeling.

REFERENCES

[1]T. D. Lee and A. U. Ebong, "A review of thin film solar cell technologies and challenges," Renew. Sustain. Energy Rev. **70**, 1286–1297 (2017).
[2]M. Green, E. Dunlop, J. Hohl-Ebinger, M. Yoshita, N. Kopidakis, and X. Hao, "Solar cell efficiency tables (version 57)," Prog. Photovolt.: Res. Appl. **29**, 3–15 (2021).
[3]M. Nakamura, K. Yamaguchi, Y. Kimoto, Y. Yasaki, T. Kato, and H. Sugimoto, "Cd-free Cu(In,Ga)(Se, S)$_2$ thin-film solar cell with record efficiency of 23.35%," IEEE J. Photovolt. **9**, 1863–1867 (2019).
[4]S. Siebentritt, "What limits the efficiency of chalcopyrite solar cells?" Sol. Energy Mater. Sol. Cells **95**, 1471–1476 (2011).
[5]D. Abou-Ras, N. Schäfer, C. J. Hages, S. Levcenko, J. Márquez, and T. Unold, "Inhomogeneities in Cu(In,Ga)Se$_2$ thin films for solar cells: Band-gap versus potential fluctuations," Solar RRL **2**, 1700199 (2018).
[6]J. H. Werner, J. Mattheis, and U. Rau, "Efficiency limitations of polycrystalline thin film solar cells: Case of Cu(In,Ga)Se$_2$," Thin Solid Films **480–481**, 399–409 (2005), eMRS 2004.
[7]T. Unold and L. Gütay, "Photoluminescence analysis of thin-film solar cells," in *Advanced Characterization Techniques for Thin Film Solar Cells* (John Wiley & Sons, Ltd., 2011), Chap. 7, pp. 151–175.
[8]A. Bauknecht, S. Siebentritt, J. Albert, and M. C. Lux-Steiner, "Radiative recombination via intrinsic defects in Cu$_x$Ga$_y$Se$_2$," J. Appl. Phys. **89**, 4391–4400 (2001).

[9]S. Shirakata, K. Ohkubo, Y. Ishii, and T. Nakada, "Effects of CdS buffer layers on photoluminescence properties of Cu(In,Ga)Se_2 solar cells," Sol. Energy Mater. Sol. Cells **93**, 988–992 (2009).
[10]K. Bothe, G. Bauer, and T. Unold, "Spatially resolved photoluminescence measurements on Cu(In,Ga)Se_2 thin films," Thin Solid Films **403–404**, 453–456 (2002).
[11]A. Redinger, S. Kretzschmar, and T. Unold, "Quantitative PL imaging of thin film solar cells—Potential and pitfalls," in *2016 IEEE 43rd Photovoltaic Specialists Conference (PVSC)* (IEEE, 2016), pp. 3559–3562.
[12]S. A. Jensen, S. Glynn, A. Kanevce, P. Dippo, J. V. Li, D. H. Levi, and D. Kuciauskas, "Beneficial effect of post-deposition treatment in high-efficiency Cu(In,Ga)Se_2 solar cells through reduced potential fluctuations," J. Appl. Phys. **120**, 063106 (2016).
[13]J. de Wild, D. G. Buldu, T. Schnabel, M. Simor, T. Kohl, G. Birant, G. Brammertz, M. Meuris, J. Poortmans, and B. Vermang, "High V_{oc} upon KF post-deposition treatment for ultrathin single-stage coevaporated Cu(In,Ga)Se_2 solar cells," ACS Appl. Energy Mater. **2**, 6102–6111 (2019).
[14]G. Bauer, L. Gütay, and R. Kniese, "Structural properties and quality of the photoexcited state in Cu($In_{1-x}Ga_x$)Se_2 solar cell absorbers with lateral submicron resolution," Thin Solid Films **480–481**, 259–263 (2005), eMRS 2004.
[15]L. Gütay, C. Lienau, and G. H. Bauer, "Subgrain size inhomogeneities in the luminescence spectra of thin film chalcopyrites," Appl. Phys. Lett. **97**, 052110 (2010).
[16]L. Gütay and G. Bauer, "Lateral variations of optoelectronic quality of Cu($In_{1-x}Ga_x$)Se_2 in the submicron-scale," Thin Solid Films **487**, 8–13 (2005).
[17]L. Gütay and G. Bauer, "Spectrally resolved photoluminescence studies on Cu(In,Ga)Se_2 solar cells with lateral submicron resolution," Thin Solid Films **515**, 6212–6216 (2007).
[18]P. Wurfel, "The chemical potential of radiation," J. Phys. C: Solid State Phys. **15**, 3967–3985 (1982).
[19]J. K. Katahara and H. W. Hillhouse, "Quasi-Fermi level splitting and sub-bandgap absorptivity from semiconductor photoluminescence," J. Appl. Phys. **116**, 173504 (2014).
[20]U. Rau and J. H. Werner, "Radiative efficiency limits of solar cells with lateral band-gap fluctuations," Appl. Phys. Lett. **84**, 3735–3737 (2004).
[21]J. Mattheis, U. Rau, and J. H. Werner, "Light absorption and emission in semiconductors with band gap fluctuations—A study on Cu(In,Ga)Se_2 thin films," J. Appl. Phys. **101**, 113519 (2007).
[22]R. Djemour, M. Mousel, A. Redinger, L. Gütay, A. Crossay, D. Colombara, P. J. Dale, and S. Siebentritt, "Detecting ZnSe secondary phase in $Cu_2ZnSnSe_4$ by room temperature photoluminescence," Appl. Phys. Lett. **102**, 222108 (2013).
[23]A. Lomuscio, T. Rödel, T. Schwarz, B. Gault, M. Melchiorre, D. Raabe, and S. Siebentritt, "Quasi-Fermi-level splitting of Cu-poor and Cu-rich $CuInS_2$ absorber layers," Phys. Rev. Appl. **11**, 054052 (2019).
[24]J. K. Larsen, S.-Y. Li, J. J. S. Scragg, Y. Ren, C. Hägglund, M. D. Heinemann, S. Kretzschmar, T. Unold, and C. Platzer-Björkman, "Interference effects in photoluminescence spectra of Cu_2ZnSnS_4 and Cu(In,Ga)Se_2 thin films," J. Appl. Phys. **118**, 035307 (2015).
[25]M. H. Wolter, B. Bissig, P. Reinhard, S. Buecheler, P. Jackson, and S. Siebentritt, "Correcting for interference effects in the photoluminescence of Cu(In,Ga)Se_2 thin films," Phys. Status Solidi C **14**, 1600189 (2017).
[26]F. Urbach, "The long-wavelength edge of photographic sensitivity and of the electronic absorption of solids," Phys. Rev. **92**, 1324 (1953).
[27]B. I. Shklovskii and A. L. Efros, "Interband absorption of light in strongly doped semiconductors," Sov. J. Exp. Theor. Phys. **32**, 733 (1971).
[28]W. Franz, "Einfluß eines elektrischen feldes auf eine optische absorptionskante," Z. Naturforsch., A **13**, 484–489 (1958).
[29]L. Keldysh, "The effect of a strong electric field on the optical properties of insulating crystals," Sov. Phys. JETP **7**, 788–790 (1958).
[30]J. K. Katahara and H. W. Hillhouse, "Erratum: "Quasi-Fermi level splitting and sub-bandgap absorptivity from semiconductor photoluminescence" [J. Appl. Phys. **116**, 173504 (2014)]," J. Appl. Phys. **119**, 239901 (2016).
[31]S. Kasap and P. Capper, *Springer Handbook of Electronic and Photonic Materials*, Springer Handbooks (Springer International Publishing, 2017).
[32]G. Rey, G. Larramona, S. Bourdais, C. Choné, B. Delatouche, A. Jacob, G. Dennler, and S. Siebentritt, "On the origin of band-tails in kesterite," Sol. Energy Mater. Sol. Cells **179**, 142–151 (2018).
[33]G. Birant, J. de Wild, T. Kohl, D. Buldu, G. Brammertz, M. Meuris, J. Poortmans, and B. Vermang, "Innovative and industrially viable approach to fabricate AlO_x rear passivated ultra-thin Cu(In,Ga)Se_2 (CIGS) solar cells," Sol. Energy **207**, 1002–1008 (2020).
[34]A. Mudryi, V. Gremenok, A. Karotki, V. Zalesski, M. Yakushev, F. Luckert, and R. Martin, "Structural and optical properties of thin films of Cu(In,Ga)Se_2 semiconductor compounds," J. Appl. Spectrosc. **77**, 371–377 (2010).
[35]J. de Wild, E. Kalesaki, L. Wirtz, and P. J. Dale, "Valence band splitting in Cu_2(Sn,Ge,Si)S_3: Effect on optical absorption spectra," Phys. Status Solidi RRL **11**, 1600410 (2017).
[36]R. Djemour, A. Redinger, M. Mousel, L. Gütay, and S. Siebentritt, "Multiple phases of $Cu_2ZnSnSe_4$ detected by room temperature photoluminescence," J. Appl. Phys. **116**, 073509 (2014).
[37]R. Djemour, A. Redinger, M. Mousel, L. Gütay, and S. Siebentritt, "Erratum: "Multiple phases of $Cu_2ZnSnSe_4$ detected by room temperature photoluminescence" [J. Appl. Phys. **116**, 073509 (2014)]," J. Appl. Phys. **118**, 089902 (2015).
[38]F. Babbe, H. Elanzeery, M. H. Wolter, K. Santhosh, and S. Siebentritt, "The hunt for the third acceptor in $CuInSe_2$ and Cu(In,Ga)Se_2 absorber layers," J. Phys.: Condens. Matter **31**, 425702 (2019).
[39]R. T. Holm, S. W. McKnight, E. D. Palik, and W. Lukosz, "Interference effects in luminescence studies of thin films," Appl. Opt. **21**, 2512–2519 (1982).
[40]J. de Wild, D. G. Buldu, T. Kohl, G. Birant, G. Brammertz, M. Meuris, J. Poortmans, and B. Vermang, "Intermediate scale bandgap fluctuations in ultrathin Cu(In,Ga)Se_2 absorber layers," J. Appl. Phys. **128**, 163102 (2020).